The long outburst of the black hole transient GRS 1716–249 observed in the X-ray and radio band

T. Bassi [1,2,3]★ M. Del Santo,[1]★ A. D'Aì,[1]★ S. E. Motta,[4] J. Malzac,[3]
A. Segreto,[1] J. C. A. Miller-Jones,[5] P. Atri,[5] R. M. Plotkin,[5] T. M. Belloni,[6]
T. Mineo[1] and A. K. Tzioumis[7]

[1] *INAF – Istituto di Astrofisica Spaziale e Fisica Cosmica di Palermo, via Ugo La Malfa 153, I-90146 Palermo, Italia*
[2] *Universitá degli Studi di Palermo, Dipartimento di Fisica e Chimica, via Archirafi 36, I-90123 Palermo, Italia*
[3] *IRAP, Université de Toulouse, CNRS, UPS, CNES, Toulouse, France*
[4] *Department of Physics, Astrophysics, University of Oxford, Denys Wilkinson Building, Keble Road, OX1 3RH Oxford, UK*
[5] *International Centre for Radio Astronomy Research – Curtin University, GPO Box U1987, Perth, WA 6845, Australia*
[6] *INAF – Osservatorio Astronomico di Brera, via E. Bianchi 46, I-23807, Merate, Italy*
[7] *CSIRO Astronomy and Space Science, Australia Telescope National Facility, PO Box 76, Epping, NSW 1710, Australia*

ABSTRACT

We present the spectral and timing analysis of X-ray observations performed on the Galactic black hole transient GRS 1716–249 during the 2016–2017 outburst. The source was almost continuously observed with the *Neil Gehrels Swift Observatory* from 2016 December until 2017 October. The X-ray hardness ratio and timing evolution indicate that the source approached the soft state three times during the outburst, even though it never reached the canonical soft spectral state. Thus, GRS 1716–249 increases the number of black hole transients showing outbursts with 'failed' state transition. During the softening events, XRT and BAT broad-band spectral modelling, performed with thermal Comptonization plus a multicolour disc black-body, showed a photon index ($\Gamma < 2$) and an inner disc temperature ($kT_{in} = 0.2$–$0.5\,\mathrm{keV}$) characteristic of the hard intermediate state. This is in agreement with the root mean square amplitude of the flux variability (rms > 10 per cent). We find that, coherently with a scenario in which the disc moves closer to the compact object, the accretion disc inner radius decreases with the increase of the inner disc temperature, until a certain point when the temperature starts to increase at constant radius. This, in addition with the spectral analysis results, suggests that either the accretion disc reached the innermost stable circular orbit during the hard intermediate state or the hot accretion flow might recondensate in an inner mini-disc. We report on the radio observations performed during the outburst finding that GRS 1716–249 is located on the radio-quiet 'outlier' branch of the radio/X-ray luminosity plane.

Key words: accretion, accretion discs – black hole physics – X-rays: binaries – X-rays: general – stars: jets.

1 INTRODUCTION

Black hole transients (BHTs) are binary systems with a black hole (BH) accreting matter from a less evolved star. They alternate quiescent periods characterized by X-ray luminosities of $L_X \sim 10^{30-33}\,\mathrm{erg\,s^{-1}}$ and episodic outbursts during which the source can reach $L_X \sim 10^{36-39}\,\mathrm{erg\,s^{-1}}$. During outbursts they can show different X-ray spectral states, characterized by different lu-

minosities (low or high), spectral shapes (hard or soft; Zdziarski & Gierliński 2004; Remillard & McClintock 2006), and timing properties (Belloni, Motta & Muñoz-Darias 2011; Belloni & Motta 2016). The spectral evolution of BHTs can be described in terms of the hardness-intensity diagram (HID; Homan & Belloni 2005) based on X-ray measurements, where the spectral states are positioned on different regions of a q-shaped pattern.

There are two main spectral states: the hard state (HS) and the soft state (SS), in which X-ray spectra are dominated by the hard X-ray emission and soft X-ray emission, respectively, and are usually explained in terms of changes in the geometry of the accretion flow on to the central object (Zdziarski 2000; Done, Gierliński &

★ E-mail: bassi@ifc.inaf.it (TB); melania.delsanto@inaf.it (MDS); antonino.dai@inaf.it (AD)

Kubota 2007). The HS corresponds to the right-hand branch of the HID, while the SS is located on the left-hand side.

BHTs start their outbursts in the HS with a spectrum well described by a power law (typical photon index $\Gamma < 2$) with a high-energy cut-off at $\sim$50–100 keV. This is physically interpreted as thermal Comptonization due to Compton up-scattering of soft disc photons by a corona of hot electrons ($\sim$100 keV) located close to the BH (Zdziarski & Gierliński 2004). A weak soft X-ray thermal component with a temperature of $\sim$0.1–0.2 keV is usually observed and interpreted as emission from an optically thick, geometrically thin, accretion disc (Shakura & Sunyaev 1973). In this state, the accretion disc is thought to be truncated at large radii (roughly $100\,R_g$) from the BH (Done et al. 2007).

During the SS, BHTs spectra show a strong soft thermal component with inner disc temperature $kT_{in} \sim 1$ keV. This emission is likely associated with the Shakura–Sunyaev disc extending down to the innermost stable circular orbit (ISCO). In addition, a steep power-law tail ($\Gamma > 2.5$), which often extends to the high energies ($\geq$500 keV), is observed. Usually, this component is interpreted as due to non-thermal Comptonization, although its origin is still debated (Poutanen & Coppi 1998; Laurent & Titarchuk 1999; Niedźwiecki & Zdziarski 2006).

Two further spectral states, namely the hard and soft intermediate states (HIMS and SIMS, respectively), are also defined (see e.g. Belloni & Motta 2016). They are located along the horizontal branches in the HID, with spectral parameters in between those of the main states.

Not all BHTs reproduce the standard q-track pattern during their outbursts: an increasing number of sources show the transition HS-to-HIMS, but never make the transitions to the SIMS and SS (Capitanio et al. 2009; Ferrigno et al. 2012; Soleri et al. 2013; Del Santo et al. 2016). These outbursts, which do not evolve through the full set of spectral states, are called 'failed' state transition. The reasons why these sources fail to make transition to the SS is still debated.

The X-ray power density spectra (PDS) of BHTs show different properties depending on the spectral state. The variability is typically quantified in terms of fractional root mean squared (rms) variability. In the HS, the fractional rms can be as high as 30 per cent (see e.g. Belloni & Motta 2016), while the SS is characterized by very low variability levels (rms < 5 per cent). During the HIMS, the fractional rms is observed to decrease from $\sim$30 per cent to 10 per cent and correlates with the hardness (Muñoz-Darias, Motta & Belloni 2011). The most dramatic changes in the power density spectra occur at the transition between the HIMS and the SIMS (Belloni & Motta 2016). This timing transition is extremely fast, as opposed to the smooth spectral changes usually observed across the HIMS to SIMS transition (Del Santo et al. 2009; Motta, Belloni & Homan 2009). The fractional rms in the SIMS is estimated to be between 7 per cent and 10 per cent (Muñoz-Darias et al. 2011).

In addition to the X/γ-ray phenomenology, the BHTs spectral states are also characterized by the production of different outflow (Mirabel 1994; Fender et al. 2006). Jets, whose emission is observed mainly in the radio band, are coupled to the accretion flow, even though the nature of this connection is still unclear. The HSs of BHTs are typically associated with a *compact* jet, characterized by a flat or slightly inverted radio spectrum (e.g. Fender et al. 2001; Corbel & Fender 2002). This is interpreted as self-absorbed synchrotron emission from steady jets, as also observed in low-luminosity AGNs (Blandford & Königl 1979). However, during the SS these compact jets are thought to be quenched (Fender et al. 1999; Corbel et al. 2000). During the HS, a radio/X-ray connection has been observed in several sources in the form of a non-linear

flux correlation $F_R \propto F_X^a$, where a $\sim$0.5–0.7, and F_R and F_X are the radio and X-ray fluxes, respectively (see e.g. Corbel et al. 2003; Gallo, Fender & Pooley 2003). In recent years, a number of Galactic BHTs were found to have a steeper correlation index, i.e. $\sim$1.4, in the radio/X-ray luminosity plane (Coriat et al. 2011; Corbel et al. 2013). They were called 'outliers', even though the increasing number of these sources could in fact turn out to be the norm (Coriat et al. 2011; Motta, Casella & Fender 2018). We refer to the 'outliers' also as radio-quiet, since they can be radio fainter by 1–2 mag around $L_X \sim 10^{36}$–10^{37} erg s^{-1}.

1.1 GRS 1716–249

The BH X-ray transient GRS 1716–249 (also known as GRO J1719–24; Nova Oph 1993) was discovered in 1993 September with the *CGRO*/BATSE and *Granat*/SIGMA telescopes (Ballet et al. 1993; Harmon et al. 1993). At that time, it reached a maximum flux of 1.4 Crab in the 20–100 keV energy band. The optical counterpart was identified with the spectral type K (or possibly later) star V2293 Oph and a distance of 2.4 ± 0.4 kpc was derived (della Valle, Mirabel & Rodriguez 1994). Masetti et al. (1996) estimated a lower limit for the compact object mass of $4.9\,M_\odot$ (confirming the BH nature), an evolved companion star mass of $1.6\,M_\odot$ and an orbital period of 14.7 hr. The hydrogen column density along the line of sight was estimated being $\sim$4 $\times$ 10^{21} atoms cm^{-2} (Tanaka 1993). In 1993 October, the source was also observed in radio by the Very Large Array (VLA), showing a flat spectrum (della Valle et al. 1993, 1994). A peculiar outburst showing five sawtooth-like shapes in the X-ray light curve was observed in 1995 (Hjellming et al. 1996). Simultaneous radio observations detected a synchrotron radio flare, implying the presence of relativistic particles and magnetic fields.

GRS 1716–249 was detected again in outburst on 2016 December 18 by *MAXI* after more than 20 yr in quiescence (Masumitsu et al. 2016; Negoro et al. 2016). Soon after, a *Neil Gehrels Swift Observatory* (hereafter *Swift*; Gehrels et al. 2004) XRT monitoring campaign (Del Santo et al. 2017a) was triggered and a preliminary spectral study showed a hard X-ray spectrum. On 2017 February 10, an *INTEGRAL* ToO of 90 ks showed that the source was in HS (Del Santo et al. 2017b). *INTEGRAL* results combined with simultaneous radio and infrared observations will be presented in a further paper.

In this paper, we present *Swift* spectral and timing analysis results and radio observations performed during the whole 2016–2017 outburst of GRS 1716–249 that lasted about 10 months.

2 X-RAY OBSERVATIONS AND DATA REDUCTION

GRS 1716–249 was observed both with the X-Ray Telescope (XRT; Burrows et al. 2005) and the Burst Alert Telescope (BAT; Barthelmy et al. 2005) on board *Swift*. XRT works in the soft X-ray band (0.2–10 keV) in four different operating modes depending on the source count rate (for more details, see Burrows et al. 2005). The Windowed Timing (WT) mode is used to obtain high time resolution light curves (1.7 ms), and it is used to observe very bright sources (1–600 mCrab). BAT is a highly sensitive coded mask instrument. It can daily observe up to 80 per cent of the whole sky in survey mode in the 15–150 keV band, aiming to catch gamma-ray burst events.

We retrieved and analysed all XRT and BAT observations performed in the period 2016 December–2017 October. We used XSPEC v. 12.9.1 for X-ray spectral analysis. Errors on spectral parameters are given at the 90 per cent confidence level.

2.1 XRT

The XRT monitoring campaign of GRS 1716–249 was performed in WT observing mode from 2017 January 28 (MJD 57781) to 2017 October 20 (MJD 58046), with target IDs 34924 and 88233 (the observation log is provided in Table 1). In observations #046, #059, and #067, the source was out of the part of the CCD used in WT mode and we therefore excluded these data from the analysis. We extracted the 0.2–10 keV count rate from each observation (see Table 1) corrected for instrumental artefacts (i.e. bad columns on the CCD) using the online products generator[1] (Evans et al. 2007, 2009). With the same tool, we extracted pointing by pointing the count rate in 0.5–2 keV and 2–10 keV energy ranges in order to study the hardness ratio (HR), defined as the ratio of the hard count rate over the soft one (see Section 4 and Fig. 1). Then, we reprocessed the XRT data using the FTOOLS software package (HEASOFT v.6.20) and the *Swift* Calibration Database (CALDB; release 20160609). We ran the task XRTPIPELINE, selecting only events with grade 0. This filter is applied in the analysis of bright sources in order to reduce the spectral distortion at low energies ($\lesssim 1.0$ keV) observed in WT mode.[2] Then we selected a circle of 20 pixel (1 pixel = 2.357 arcsec) radius centred on the source position to extract the spectra using the task XRTPRODUCTS. When the source was on the edge of the CCD, we selected a region with the largest size possible; in pointings #054, #058, and #060, radii of 5, 8, and 4 pixels, respectively, were chosen. The background was extracted from a region of the same size of the source region located away from the source.

According to Romano et al. (2006) the pile-up correction should be applied for sources with count rate above 100 ct s^{-1}. However, we have evaluated that pointings with count rate between 90 and 100 ct s^{-1} were still affected by pile-up.[3] Thus, the pile-up correction was carried out for observations with count rate (values plus uncertainties) ≥ 90 ct s^{-1} (see Table 1). For these observations, we extracted the spectra from an annular region centred on the source with an outer radius of 20 pixels and an inner radius of 3 pixels. In order to apply the χ^2 statistics we grouped the channels for having at least 50 counts per energy bin. We computed power spectra in the energy band 0.4–10.0 keV from each XRT observation, using custom software written in IDL.[4] We used ≈ 29-s long intervals and a Nyquist frequency of ≈ 280 Hz. We averaged the PDS in order to obtain one PDS per observation, which we normalized according to Leahy, Elsner & Weisskopf (1983). We measured the fractional rms in the frequency range of 0.035–10 Hz. After MJD 58000 (2017 September 4), the source count rate was too low ($\lesssim 5$ counts s^{-1}) to allow us to measure the fractional rms, the upper limit to which is essentially 100 per cent. For this reason, we do not report any fractional rms value after this date.

2.2 BAT

GRS 1716–249 was almost daily observed in survey mode with BAT from 2016 December 1 (MJD 57723). We processed the BAT data, available from the HEASARC public archive, using the BAT-IMAGER software (Segreto et al. 2010). This software performs screening, mosaicking and source detection, and produces scientific products for any detected source. We used the official BAT spectral redistribution matrix.

We extracted the light curves in two energy bands (15–30 keV and 30–90 keV) in order to compute the HR, defined as the count rate ratio [30–90] keV/[15–30] keV, with one-day time interval. Spectra were extracted in 30 channels with logarithmic binning in the energy range 15–185 keV. Due to the poor statistics of the hard X-ray emission at the beginning of the outburst, data from MJD 57723 until MJD 57739 were excluded.

3 RADIO OBSERVATIONS AND DATA REDUCTION

3.1 Australia Telescope Compact Array

We observed GRS 1716–249 with the Australia Telescope Compact Array (ATCA) from 18:52–21:00 UTC on 2017 February 9, under programme code C2538. We observed simultaneously in two 2-GHz bands, centred at 5.5 and 9.0 GHz, with the array in its extended 6D configuration, with a maximum baseline of 6 km. We used PKS $1934 - 638$ as our amplitude and bandpass calibrator, and PKS $1710 - 269$ ($2.4°$ from GRS 1716–249) as our complex gain calibrator, adopting a cycle time of 16.5 min, with 15 min spent on GRS 1716–249 and 1.5 min on the calibrator in each cycle. Data reduction was performed according to standard procedures in the Multichannel Image Reconstruction, Image Analysis, and Display MIRIAD software package (Sault, Teuben & Wright 1995). The calibrated data were imported into the Astronomical Image Processing System (AIPS; Greisen 2003) for imaging, where we used pure uniform weighting to minimize the elongation of the synthesized beam that arose from the sparse *uv*-coverage. Following deconvolution, the source flux density was measured by fitting a point source in the image plane.

3.2 Long Baseline Array

We observed GRS 1716–249 with the Australian Long Baseline Array (LBA) on three occasions, 2017 February 21, April 22, and August 13, under programme code V447. The first two observations were taken outside formal LBA sessions, with a minimal array of just four antennas. However, the August 13 observation was taken during an official LBA run, allowing us to include 10 stations in the array. Details of the different observations are given in Table 2.

Data were correlated using the DIFX software correlator (Deller et al. 2011), and reduced using standard procedures within AIPS. Given the faintness of the target, we observed in phase referencing mode, nodding between GRS 1716–249 and the nearby phase reference calibrator J1711–2509, located $1.87°$ from GRS 1716–249. In each cycle, we spent 90 s on the calibrator and 210 s on the target. Every fifth target scan was substituted for a scan on a nearby check source, J1713–2658. Amplitude calibration was performed using the system temperatures recorded at the individual stations where available, and nominal values in other cases. We used a bright fringe finder source to perform instrumental phase and delay corrections, and subsequently to calibrate the instrumental frequency response. We imaged and self-calibrated the phase reference source, before using it to derive the time-dependent amplitude, phase, delay, and rate solutions, which were applied to GRS 1716–249. After imaging the target source, its flux density was determined by fitting a point source in the image plane, since in no case was it observed to be extended. The loss of one antenna (Cd) for

---

[1] http://www.swift.ac.uk/user_objects/

[2] http://www.swift.ac.uk/analysis/xrt/digest_cal.php

[3] http://www.swift.ac.uk/analysis/xrt/pileup.php

[4] GHATS, http://www.brera.inaf.it/utenti/belloni/GHATS_Package/Home.html

Table 1. XRT pointings of GRS 1716–249 analysed in this work. The columns are (1) sequence number, (2) start time in Terrestrial Time (TT), (3) exposure time, (4) 0.2–10 keV count rate and errors obtained using the online products generator (Evans et al. 2007, 2009). In columns (5) and (6), we report the photon index and the reduced chi squared, respectively, obtained by fitting spectra with an absorbed power-law model (see Section 4).

Seq # (1)	Start time (2)	Exposure (s) (3)	Count rate (ct s^{-1}) (4)	Γ (5)	χ^2_ν(dof) (6)
001[a]	2017-01-28 00:08:01	992	93.1 ± 0.4	$1.55^{+0.03}_{-0.03}$	1.08(342)
002[a]	2017-01-29 19:08:57	999	102 ± 3	$1.57^{+0.04}_{-0.05}$	0.93(315)
003[a]	2017-01-31 00:05:15	683	95 ± 2	$1.58^{+0.04}_{-0.04}$	1.10(248)
004[a]	2017-02-02 17:31:57	990	100 ± 4	$1.60^{+0.03}_{-0.03}$	1.04(372)
005[a]	2017-02-04 18:56:10	924	100.2 ± 0.3	$1.58^{+0.03}_{-0.03}$	1.03(373)
006[a]	2017-02-06 10:59:09	305	96 ± 1	$1.53^{+0.06}_{-0.05}$	0.95(138)
007[a]	2017-02-08 04:15:42	946	97.9 ± 0.3	$1.59^{+0.03}_{-0.03}$	1.12(384)
008[a]	2017-02-09 02:19:11	1478	80 ± 12	$1.62^{+0.03}_{-0.03}$	1.07(432)
009[a]	2017-02-09 05:43:11	1282	87 ± 11	$1.57^{+0.03}_{-0.03}$	1.02(365)
010[a]	2017-02-09 09:01:44	1451	97.4 ± 0.3	$1.62^{+0.03}_{-0.02}$	1.03(452)
011[a]	2017-02-09 13:27:07	1287	102 ± 1	$1.64^{+0.03}_{-0.03}$	1.14(400)
012[a]	2017-02-09 18:11:07	1360	103 ± 3	$1.64^{+0.03}_{-0.03}$	0.89(364)
013[a]	2017-02-09 21:27:58	1367	103 ± 0.7	$1.62^{+0.03}_{-0.03}$	1.00(425)
014[a]	2017-02-11 07:11:47	949	101 ± 3	$1.57^{+0.04}_{-0.03}$	0.99(299)
015[a]	2017-02-12 13:17:33	1209	81 ± 12	$1.57^{+0.03}_{-0.03}$	1.06(431)
016[a]	2017-02-14 08:42:43	921	87 ± 4	$1.55^{+0.03}_{-0.03}$	1.10(322)
017[a]	2017-02-14 19:35:14	975	91.6 ± 0.4	$1.60^{+0.03}_{-0.03}$	0.99(358)
018[a]	2017-02-16 03:30:55	997	90.2 ± 0.3	$1.59^{+0.03}_{-0.03}$	1.17(357)
019[a]	2017-02-22 13:56:26	1734	92 ± 5	$1.57^{+0.03}_{-0.03}$	1.05(398)
020[a]	2017-02-24 09:00:33	966	100.3 ± 0.3	$1.56^{+0.03}_{-0.03}$	1.19(362)
021[a]	2017-02-26 15:27:03	934	100.1 ± 0.3	$1.60^{+0.03}_{-0.03}$	1.05(348)
022[a]	2017-03-09 12:48:10	1063	97.4 ± 0.4	$1.63^{+0.03}_{-0.03}$	1.04(375)
024[a]	2017-03-15 18:46:20	985	90.2 ± 0.3	$1.59^{+0.03}_{-0.03}$	1.08(348)
025[a]	2017-03-21 20:16:46	959	98.7 ± 0.3	$1.67^{+0.03}_{-0.03}$	0.92(384)
026[a]	2017-03-27 22:36:50	940	124 ± 11	$1.69^{+0.03}_{-0.03}$	0.92(333)
027[a]	2017-04-02 09:07:26	960	128 ± 6	$1.76^{+0.03}_{-0.03}$	1.09(389)
029[a, b]	2017-04-07 08:50:41	1664	131 ± 1	$1.85^{+0.02}_{-0.02}$	1.21(511)
030[a, b]	2017-04-08 23:11:36	965	131.0 ± 0.7	$1.93^{+0.05}_{-0.03}$	1.33(413)
031[a, b]	2017-04-10 21:12:42	1933	143 ± 6	$2.01^{+0.02}_{-0.02}$	1.19(514)
032[a, b]	2017-04-11 03:50:28	727	147 ± 3	$2.06^{+0.03}_{-0.03}$	1.20(383)
033[a, b]	2017-04-12 11:26:48	1852	137 ± 3	$1.98^{+0.02}_{-0.02}$	1.23(508)
034[a, b]	2017-04-14 00:37:03	929	123 ± 7	$1.92^{+0.03}_{-0.03}$	1.13(351)
035[a]	2017-04-21 01:39:30	444	98.1 ± 0.5	$1.75^{+0.04}_{-0.04}$	1.07(236)
036	2017-05-05 17:42:16	1152	83 ± 0.3	$1.72^{+0.02}_{-0.02}$	1.17(525)
037	2017-05-11 01:28:31	1258	79.2 ± 0.3	$1.71^{+0.02}_{-0.02}$	1.03(538)
038[a, b]	2017-05-22 22:52:31	839	100.3 ± 0.4	$1.90^{+0.03}_{-0.03}$	1.11(333)
039[a]	2017-05-26 17:55:22	724	91.8 ± 0.5	$1.79^{+0.04}_{-0.04}$	1.15(261)
040	2017-06-02 12:29:01	354	78.6 ± 0.5	$1.79^{+0.03}_{-0.03}$	0.99(295)
041	2017-06-07 00:25:55	1059	74.8 ± 0.3	$1.75^{+0.02}_{-0.02}$	1.20(486)
042	2017-06-12 04:46:37	3354	75.4 ± 0.9	$1.81^{+0.01}_{-0.01}$	1.15(641)
043	2017-06-17 02:58:56	1058	76 ± 1	$1.82^{+0.02}_{-0.02}$	1.17(475)
044	2017-06-23 21:29:38	1033	74.0 ± 0.3	$1.91^{+0.02}_{-0.02}$	1.13(464)
045[a, b]	2017-06-30 20:57:38	437	91 ± 4	$2.13^{+0.04}_{-0.04}$	1.29(267)
046†	2017-07-09 18:39:24	964	–	–	–
047[b]	2017-07-16 03:43:26	978	66.9 ± 0.3	$2.12^{+0.02}_{-0.02}$	1.31(413)
048[a, b]	2017-07-23 11:12:15	988	100.1 ± 0.3	$2.64^{+0.04}_{-0.04}$	1.35(295)
049[a, b]	2017-07-25 15:33:47	980	106.0 ± 0.3	$2.68^{+0.04}_{-0.04}$	1.30(286)
050[a, b]	2017-07-26 17:10:39	1491	110.6 ± 0.3	$2.79^{+0.03}_{-0.03}$	1.34(349)

Table 1 – *continued*

Seq # (1)	Start time (2)	Exposure (s) (3)	Count rate (ct s^{-1}) (4)	Γ (5)	χ^2_ν(dof) (6)
051^b	2017-07-29 20:00:17	972	80.6 ± 0.3	$2.57^{+0.02}_{-0.02}$	1.41(404)
052^b	2017-07-30 18:30:24	973	78.3 ± 0.3	$2.55^{+0.02}_{-0.02}$	1.42(397)
053^b	2017-07-31 22:58:09	919	74.7 ± 0.3	$2.53^{+0.03}_{-0.03}$	1.46(388)
054$^{b,\,c}$	2017-08-06 19:19:08	863	20.8 ± 0.2	$1.95^{+0.04}_{-0.04}$	0.99(229)
055^b	2017-08-11 06:27:11	817	28.7 ± 0.2	$1.87^{+0.04}_{-0.04}$	0.99(263)
056	2017-08-13 09:08:40	1081	23.1 ± 0.2	$1.81^{+0.04}_{-0.03}$	1.17(277)
057	2017-08-15 05:46:59	1058	21.4 ± 0.1	$1.74^{+0.04}_{-0.04}$	0.95(252)
058^c	2017-09-08 03:38:00	1667	4.24 ± 0.07	$1.58^{+0.07}_{-0.06}$	0.93(107)
059†	2017-09-11 01:47:00	1529	–	–	–
060^c	2017-09-15 00:05:15	1226	2.85 ± 0.08	$1.52^{+0.11}_{-0.10}$	0.89(51)
061	2017-09-17 00:05:15	1106	3.31 ± 0.07	$1.58^{+0.11}_{-0.10}$	0.95(45)
062	2017-09-21 01:07:13	1639	3.24 ± 0.06	$1.55^{+0.07}_{-0.07}$	0.95(94)
063	2017-10-01 00:10:50	1425	4.09 ± 0.06	$1.47^{+0.08}_{-0.07}$	0.99(84)
064	2017-10-05 01:25:00	1591	4.29 ± 0.07	$1.56^{+0.09}_{-0.08}$	1.29(69)
065	2017-10-10 00:57:59	1372	3.61 ± 0.06	$1.63^{+0.10}_{-0.09}$	1.05(68)
066	2017-10-15 00:33:11	1477	3.66 ± 0.06	$1.61^{+0.08}_{-0.08}$	1.27(75)
067†	2017-10-20 11:21:50	1388	–	–	–
ID 88233001$^{a,\,b}$	2017-07-28 16:51:27	3716	100.0 ± 0.2	$2.75^{+0.02}_{-0.02}$	1.57(481)

Notes:

†Observations not used since GRS 1716–249 was out of the part of the CCD used in WT mode.

^{a}Pile-up correction has been applied.

^{b}Spectral fits need an additional component (i.e. DISKBB, see Section 4.3) to the simple power-law.

^{c}Spectrum has been extracted in a region of radius smaller than 20 pixels since the source was on the edge of the CCD.

the majority of the first observation (2017 February 21) meant that imaging with three antennas could not reliably reproduce the source structure, so for this epoch we fit the data with a point source in the *uv*-plane.

3.3 Very Large Array

We observed GRS 1716–249 with the Karl G. Jansky Very Large Array (VLA) from 05:48–06:35 UTC on 2017 August 12, under programme code SI0462. The array was in its moderately compact C configuration, and we split the antennas into two subarrays of 14 and 12 antennas, each of which observed simultaneously in two 1-GHz basebands, centred at 5.25 and 7.45 GHz, and 8.8 and 11.0 GHz, respectively. GRS 1716–249 was setting during the observations, with an elevation decreasing from 19° to 14°. The weather was poor, with overcast skies, light rain and thunderstorms over the array leading to poor atmospheric phase stability. Combined with the low elevation, this led to significant phase decorrelation, even at frequencies as low as 5 GHz.

We used 3C 286 as our flux and bandpass calibrator, and J1751 − 2524 as our complex gain calibrator. We conducted two 17.5-min scans on GRS 1716–249 each of which was bracketed by a 1-min scan on the complex gain calibrator. Data reduction was carried out following standard procedures within the Common Astronomy Software Application (CASA; McMullin et al. 2007). We imaged the calibrated data using Briggs weighting, with a robust parameter of 1. The image noise levels we achieved were significantly higher than expected theoretically (by factors of 2–4, increasing with frequency). We attribute this to the higher system temperatures arising

from the poor weather. GRS 1716–249 was significantly detected at all frequencies, and we determined the source flux density by fitting it with a point source in the image plane.

Given the weather conditions at the array, we used the middle scan on the complex gain calibrator to quantify the extent of the phase decorrelation. We re-reduced the data, using only the first and last calibrator scans to solve for the complex gain solutions, treating the middle calibrator scan as a second target. A comparison of the calibrator flux densities when treated as a target (interpolating the gain solutions from the initial and final scans) showed that the peak amplitudes were lower by 9.6 per cent, 14.3 per cent, 25.7 per cent, and 32.3 per cent at 5.25, 7.45, 8.8, and 11.0 GHz, respectively. We therefore corrected the fitted flux densities of GRS 1716–249 by these factors to derive the final flux densities, as detailed in Table 3.

4 RESULTS

The XRT and BAT count rate and HR evolution of GRS 1716–249 are shown in Fig. 1. We noted three peaks in the XRT light curves (panel *a* in Fig. 1) which reach their maximum on MJD 57854.16 (#032) with a total of 143 ct s^{-1}, on MJD 57895.95 (#038) with 97 ct s^{-1} and on MJD 57960.72 (#050) with 103 ct s^{-1}. They correspond to dips in the BAT light curves (panel *c* in Fig. 1) and in both the HRs (panels *b* and *d* in Fig. 1), and clearly indicate a spectral softening. The third peak corresponds to the softest observed episode: the 2–10 keV count rate was lower than the 0.5–2 keV count rate by a factor of 2, whereas it was of 30 per cent and 20 per cent for the first two peaks.
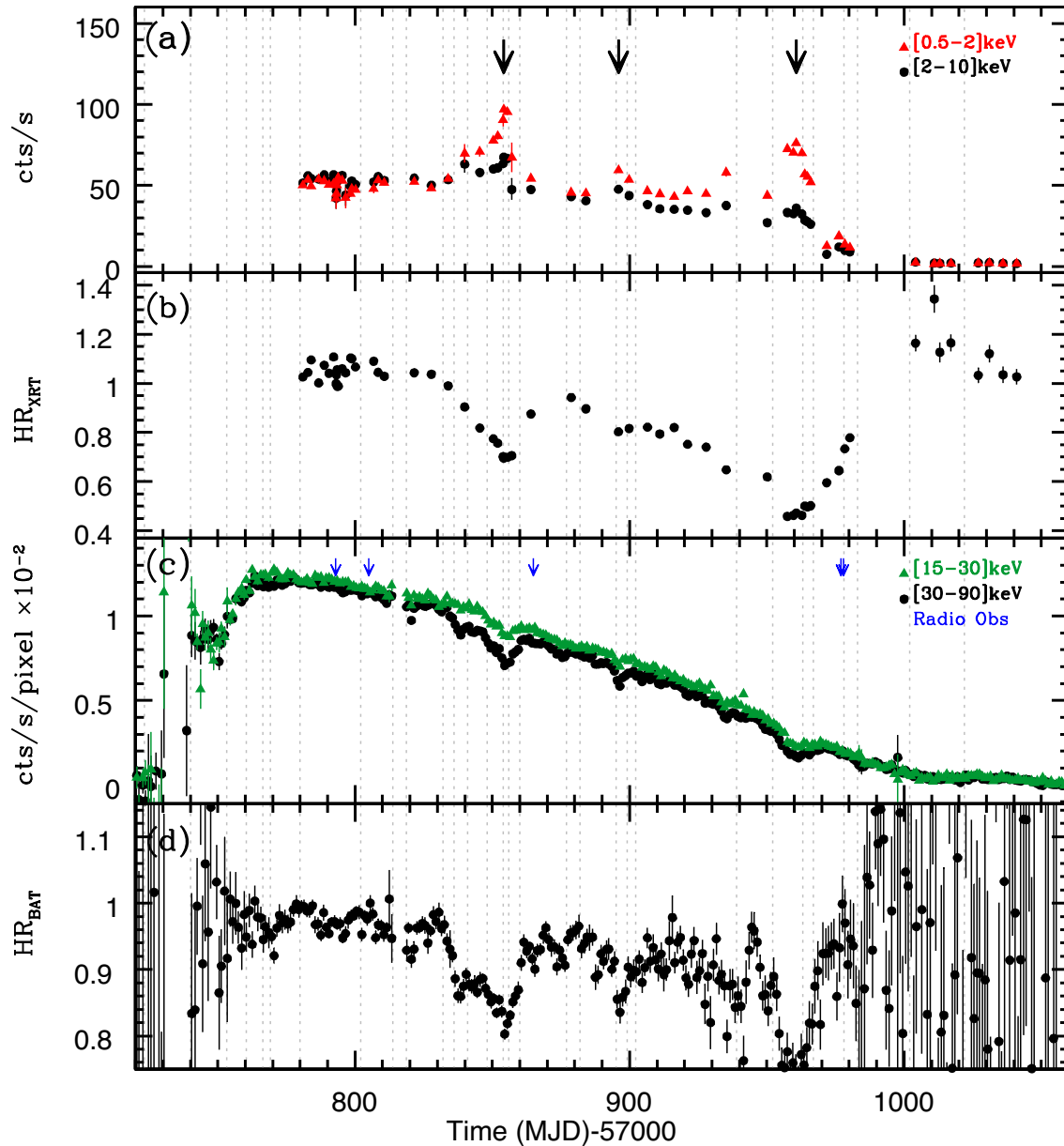
Figure 1. XRT light curves in the 0.5–2 keV and 2–10 keV energy ranges, extracted by pointing (panel *a*), plotted with the corresponding hardness ratio (panel *b*). In panel *c*, we show the 15–30 and 30–90 keV light curves observed by BAT, with a 1-d binning time, and the related hardness ratio (panel *d*). Dashed lines indicate the GTI considered for the broad-band spectral analysis. In the XRT light curve, three strong peaks at MJD 57857.03, 57906.52, and 57964.77 (marked with black arrows) in correspondence to dips in the BAT light curve and in the hardness ratios have been observed. This indicates softening in the X-ray spectra.

Table 2. LBA observations of GRS 1716−249. Station codes are At (the phased-up ATCA); Cd (Ceduna); Ho (Hobart); Ke (Katherine); Mp (Mopra); Pa (Parkes); Td (the 34m DSS36 antenna at Tidbinbilla); Ti (the 70m DSS43 antenna at Tidbinbilla); Ww (the Warkworth 12m antenna); Yg (Yarragadee).

Programme code	Date, Time (UT)	MJD	Bandwidth	Array
V447D	2017-02-21, 17:18–02:30	57805.91 ± 0.19	1×64 MHz	At-Cd-Ho-Mp
V447E	2017-04-22, 11:56–23:00	57865.73 ± 0.23	4×16 MHz	At-Cd-Ho-Mp
V447F	2017-08-13, 06:56–16:00	57978.48 ± 0.19	4×16 MHz	At-Cd-Ho-Ke-Mp-Pa-Td-Ti-Wa-Yg

Table 3. Measured radio flux densities of GRS 1716–249. Quoted uncertainties are statistical only. Nominal systematic uncertainties are of order 5 per cent for the VLA and ATCA, and at least 10 per cent for the LBA. VLA flux densities have been corrected for the measured phase decorrelation, as described in Section 3.3.

Array	Date	MJD	Frequency (GHz)	Flux density (mJy)	Spectral index
ATCA	2017 Feb 9	57793.835 ± 0.040	5.5	3.28 ± 0.05	-0.15 ± 0.19
ATCA	2017 Feb 9	57793.835 ± 0.040	9.0	3.04 ± 0.03	–
LBA	2017 Feb 21	57805.911 ± 0.192	8.4	1.28 ± 0.15	–
LBA	2017 Apr 22	57865.729 ± 0.225	8.4	1.13 ± 0.11	–
VLA	2017 Aug 12	57977.256 ± 0.014	5.25	0.63 ± 0.04	-0.07 ± 0.19
VLA	2017 Aug 12	57977.256 ± 0.014	7.45	0.48 ± 0.05	–
VLA	2017 Aug 12	57977.256 ± 0.014	8.8	0.68 ± 0.11	–
VLA	2017 Aug 12	57977.256 ± 0.014	11.0	0.70 ± 0.14	–
LBA	2017 Aug 13	57978.479 ± 0.188	8.4	0.29 ± 0.04	–

In Fig. 2 (top panel), we show the XRT HID of GRS 1716–249. We plotted the total 0.5–10 keV count rate versus the count rate ratio 2–10 keV/0.5–2 keV. It is worth noting that due to the late XRT trigger with respect to the outburst beginning (the XRT monitoring started a few days after the hard X-ray peak), the HS right-hand branch in the HID was missed and the GRS 1716–249 q-track starts from the bright HS. The outburst evolved towards the intermediate states (IMS) on the horizontal branch. The three soft X-ray peaks in the XRT light curves are shown on the HID with a purple triangle, a green diamond and a magenta square. The X-ray spectra of GRS 1716–249 are observed to soften and harden twice along the IMS branch, until it reaches the softest observed state (magenta square), then the flux starts to decrease and the source simultaneously becomes harder along a diagonal track. We noted that the shape of this HID is different from that observed in the majority of BHTs (e.g. GX 339-4, Belloni et al. 2006; Dunn et al. 2010). Indeed, there is not a clear SS branch on the left side of the diagram as observed in H 1743–322 and MAXI J1836–194 by Capitanio et al. (2009) and Ferrigno et al. (2012), respectively.

4.1 *XRT* temporal variability

In BHTs the fractional rms of the variability is related to the spectral state (Muñoz-Darias et al. 2011). Therefore, we studied the evolution of the fractional rms during the GRS 1716–249 outburst (Fig. 2, bottom panel). We noted that the fractional rms measured from the XRT data is not directly comparable with those from *RXTE*/PCA (Muñoz-Darias et al. 2011), because of the different energy bands which the two instruments are sensitive to. However, the overall behaviour of the fractional rms measured with XRT is expected to be similar to that would be measured by *RXTE* (with a difference in normalization). In the first XRT observations GRS 1716–249 showed fractional rms between 25 per cent and 30 per cent (e.g. cyan dot), typical of the bright HS at the beginning of the HIMS branch. Then, after MJD 57830, the fractional rms started to decrease down to a value of 17 per cent (MJD 57854), which corresponds to the purple triangle in the HID (Fig. 2, top panel) and to the first dip in the HRs (Fig. 1 b and d). Afterwards, the fractional rms increased again up to values of about 25 per cent, then a second dip (green diamond) with fractional rms of 20 per cent at MJD 57896 (corresponding to the second softening) occurred. Simultaneously with the third HR softening, the fractional rms decreased down to 12 per cent (magenta square, at MJD 57961). Finally, it rose back to 40 per cent in

the final part of the outburst, indicating that the source returned to the HS.

4.2 XRT spectral analysis

We fit each XRT spectrum in the 0.5–10 keV energy band with an absorbed (TBABS in XSPEC) power-law model with Wilms, Allen & McCray (2000) cosmic abundances and Verner et al. (1996) cross-sections for the interstellar absorption. In Fig. 3, we show the evolution of the spectral parameters. N_H shows values around $(0.6\text{–}0.7) \times 10^{22}$ cm^{-2}, with a peak value at $\sim 0.9 \times 10^{22}$ cm^{-2} (MJD 57960.72). The photon index (Γ) remains between 1.5 and 1.7 throughout the whole outburst, with the exception of significant increases during the three XRT peaks and BAT dips observed over the periods of spectral softening (Fig. 1). The XRT spectrum corresponding to the first peak (2017 April 11, #032) shows a photon index $\Gamma \sim 2.1$, while on May 22 (#038) we obtained a photon index of ~ 1.9. The source reached its steepest spectral slope on July 26 (#050) with $\Gamma \sim 2.8$, corresponding to the lowest HR value and the highest $N_H \sim 0.9 \times 10^{22}$ cm^{-2}, even though the reduced χ^2 is not statistically acceptable (see Table 1). The large column density variations derived could be caused by the inadequacy of our model, i.e. an accretion disc could be required to fit the data. We therefore added a multicolour disc black-body (DISKBB in XSPEC) component to the previous model in all spectra with $\chi_\nu^2 > 1.1$. We estimated with the F-test that this component is required by all spectra with $\Gamma \geq 1.8$. However, we noted that in a few spectra where $\Gamma < 1.8$ with $\chi_\nu^2 > 1.1$, the bad residuals are due to the known strong instrumental silicon (1.84 keV) and gold (2.2 keV) edges,[5] so these fits can be considered acceptable.

4.3 Broad-band X-ray spectra

We improved the spectral analysis by adding averaged BAT spectra in order to perform a broad-band fit. Using the light curves and HRs (see Fig. 1), we selected good time intervals (GTIs, see Table 4) based on two selection criteria: (1) constant HR in both BAT and XRT, (2) BAT flux variation lower than 20 per cent, with the exception of the two last intervals where the variation is about 30 per cent. We point out that there are a number of BAT

[5] https://heasarc.gsfc.nasa.gov/docs/heasarc/caldb/swift/docs/xrt/SWIFT-XRT-CALDB-09_v19.pdf
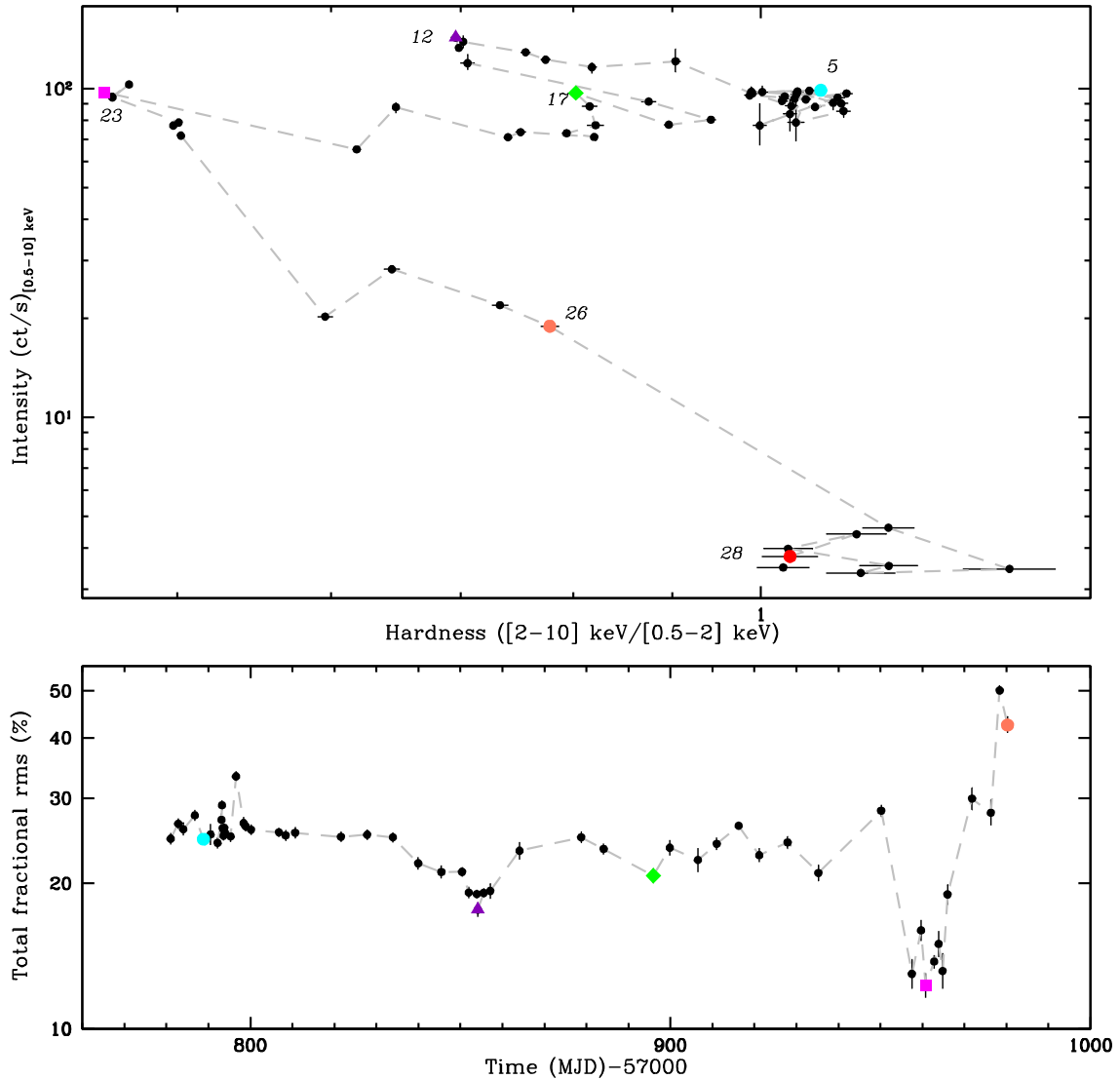
Figure 2. *Top panel:* HID The coloured dots are associated with the broad-band spectra shown in Fig. 5. The outburst has been observed by XRT when GRS 1716−249 was at the top-right side of the pattern (cyan dot, broad-band spectrum *5*), then it evolves along the horizontal branch (purple triangle, spectrum *12*). It reaches the softest state (magenta square, spectrum *23*) and then takes a diagonal trajectory (orange dot, spectrum *26*) on its return to the HS (red dot, spectrum *28*), before going in quiescence. The magenta square, purple triangle, and green diamond correspond to the softest points in each of the three softening episodes. *Lower panel:* XRT fractional rms evolution. The soft points observed in the HID correspond to fractional rms values typical of the HIMS (10–30 per cent, Muñoz-Darias et al. 2011).

GTIs averaged spectra that do not overlap with any XRT observations. On the other hand, we selected one XRT spectrum for each GTI, making sure that it was consistent, in terms of spectral parameters and flux, with the other XRT spectra within the same GTI. In the broad-band spectra, we introduced a systematic error of 2 per cent according to the instrument calibration guidelines.

The broad-band spectra were fitted with an absorbed thermal Comptonization model (TBABS plus NTHCOMP in XSPEC, see Table 4). We assumed that the seed photons followed a disc black-body distribution (parameter *inp_type* = 1) and we fixed the seed photon temperature at 0.1 keV every time the disc black-body component was not required. We verified that the DISKBB component, when required, improved our fits significantly (*F*-test values always lower than 8×10^{-5}). When fitting all spectra with a constant N_H, we noticed statistically significant discrepancies in the residuals of

several spectra, so that we left this parameter free to vary. However, we fitted simultaneously the nine spectra in which the disc component was required, keeping the N_H tied (see Table 4).

The photon index varies from 1.6 up to 1.9 (see panel a in Fig. 4), while the electron temperature (kT_e, see panel b in Fig. 4) is well constrained when the source is bright in hard X-ray. However, in some cases, in particular during the last spectral softening, we only obtained a lower limit on this parameter. Extra components in addition to the thermal Comptonization could play a role (i.e. non-thermal Comptonization, reflection) in the IMS. Nevertheless, the BAT statistics and the poor high energy coverage do not allow us to disentangle the X-ray continuum of BHTs.

The thermal disc component is well detected in the spectra collected during the three peaks observed in the XRT light curve. The inner disc temperature (kT_{in}) varies between 0.2 and 0.5 keV, the latter was observed during the third peak softening (see panel c in
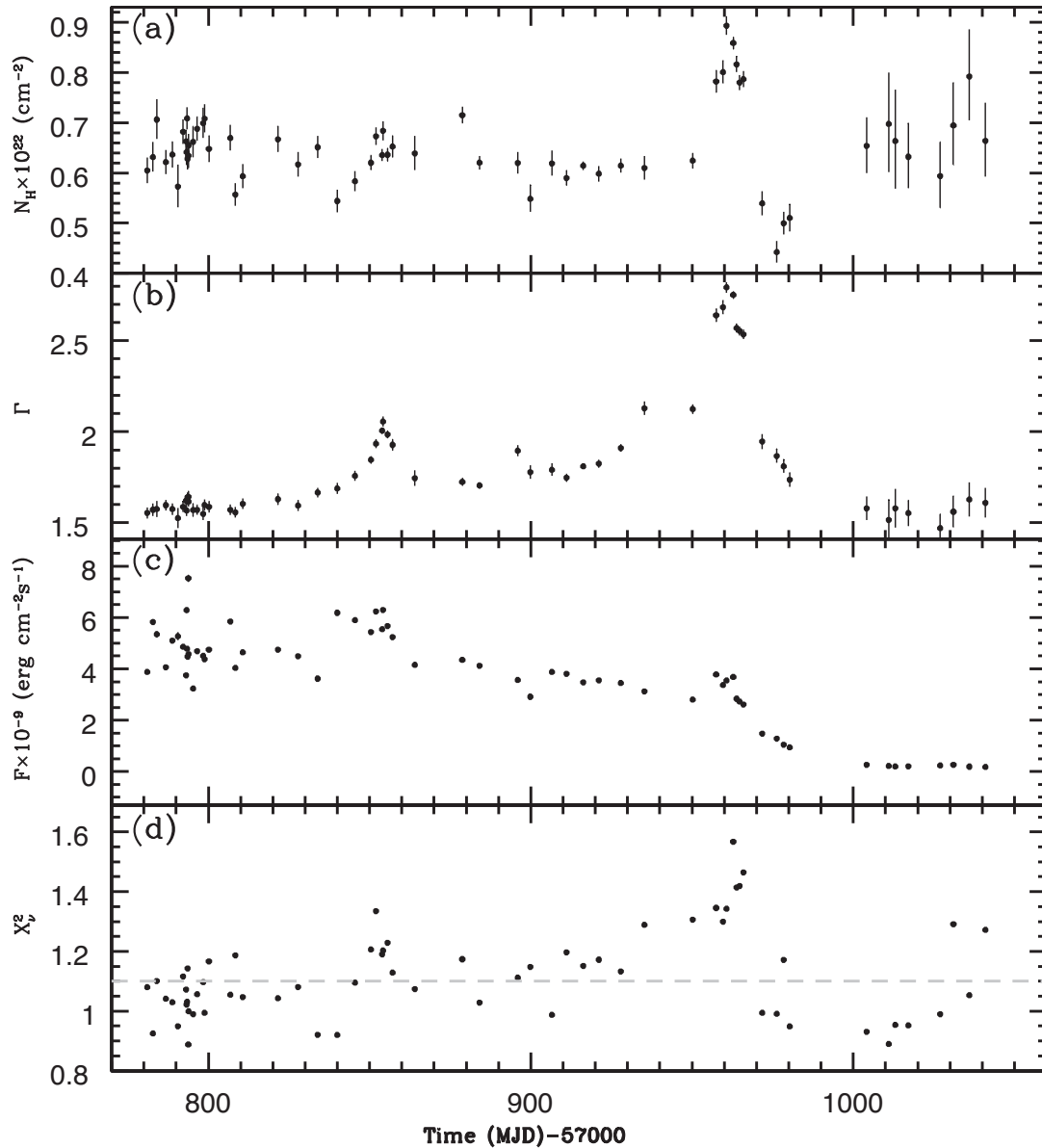
Figure 3. Parameters of the XRT spectra fitted with an absorbed power-law model (TBABS∗PO). From the top to the bottom panel: (a) hydrogen column density in units of 10^{22} cm^{-2}, (b) photon index, (c) 0.5–10 keV absorbed flux in units of 10^{-9} er g cm^{-2} s^{-1}, and (d) reduced χ^2. The high variation of N_H is due to a non-adequate spectral modelling. The spectra with a $\chi^2_\nu > 1.1$ and $\Gamma \geq 1.8$ require an additional multicolour disc black-body (DISKBB) component.

Fig. 4). Our findings are in agreement with Muñoz-Darias et al. (2011) who found that the presence of the accretion disc is detected when the fractional rms is ∼20 per cent. In the spectra collected during the peak of the three softenings (spectra *12*, *17*, and *23* in Table 4), we estimated that the disc flux contributes 9 per cent, 5 per cent, and 34 per cent, respectively, to the total unabsorbed bolometric flux of GRS 1716–249. In Fig. 5, we show energy spectra, models, and residuals for six representative observations: the three softening peaks (HIMS), one bright HS spectrum (*5*), one HIMS spectrum collected during the outburst decreasing phase (*26*) and a HS spectrum (*28*) collected before the source quiescence.

In addition, we have estimated the inner disc radius as a function of the inclination angle (see Table 4) from the DISKBB normalization. Then we applied the correction factor between the apparent and true inner radius by Kubota et al. (1998) and the hardening factor of 1.7 (Shimura & Takahara 1995). In Fig. 6 (left), we plot R_{in}

$(\cos\vartheta)^{1/2}$ (hereafter R_c) versus kT_{in} that shows that most of our measurements are consistent with a constant radius $R_c \sim 15$ km. There is only one point (at lower temperature) that appears to have a significantly higher inner disc radius and a second point with a value (∼23 km) that is not consistent with the mean radius. We also estimated whether the disc luminosity varies as a function of the inner disc temperature according to $L \propto T^4$. In Fig. 6 (right), we plot the observed disc flux and temperature against each other for all observations where R_c was almost constant. The power-law index from the best fit is $\alpha = 4.2 \pm 1.0$ (χ^2(dof) $= 4.5(5)$). The probability to have the χ^2 obtained is of 0.52 per cent. This suggests that the inner disc temperature variations are driven only by changes in mass accretion rate at constant inner disc radius, and appears inconsistent with a varying inner disc radius at constant mass accretion rate ($L \propto T^{4/3}$; Done et al. 2007). This is particularly evident within the third softening when a flux variation of about a factor of 3 is

Table 4. Good Time Intervals and best-fitting parameters of the broad-band XRT and BAT spectra performed with an absorbed thermal Comptonization (NTHCOMP) model and a disc black-body model (DISKBB) when required. (1) Number of the spectrum, (2) sequence number of the XRT pointing selected within the BAT GTI, start (3) and stop (4) time of the GTI in MJD, (5) hydrogen column density in units of 10^{22} cm^{-2}, (6) photon index, (7) Comptonizing electron temperature in keV, (8) inner disc temperature, (9) inner disc radius, (10) unabsorbed bolometric flux (0.1–500 keV), disc and Comptonized component fluxes, (11) reduced χ^2.

n	Seq. (#)	MJD start	MJD stop	$N_{\rm H} \times 10^{22}$ (cm^{-2})	Γ	$kT_{\rm e}$ (keV)	$kT_{\rm in}$ (keV)	$R_{\rm in}\,(\cos\vartheta)^{1/2}$ (km)	Flux $\times 10^{-8}$ (erg cm^{-2} s^{-1}) Bol	Disc	Comp	χ_r^2(dof)
(1)	(2)	(3)	(4)	(5)	(6)	(7)	(8)	(9)		(10)		(11)
1	–	57740.08	57752.85	–	$1.69^{+0.05}_{-0.05}$	>57	–	–	2.01	–	2.01	1.22(25)
2	–	57753.24	57757.49	–	$1.68^{+0.04}_{-0.04}$	>50	–	–	2.26	–	2.26	1.01(25)
3	–	57760.41	57766.39	–	$1.69^{+0.02}_{-0.02}$	55^{+12}_{-8}	–	–	2.51	–	2.51	0.91(25)
4	–	57769.24	57779.96	–	$1.69^{+0.01}_{-0.01}$	53^{+5}_{-4}	–	–	2.54	–	2.54	0.97(25)
5	005	57780.01	57801.96	$0.69^{+0.02}_{-0.02}$	$1.67^{+0.01}_{-0.01}$	48^{+4}_{-3}	–	–	2.37	–	2.37	1.01(399)
6	020	57802.01	57813.70	$0.61^{+0.02}_{-0.02}$	$1.65^{+0.01}_{-0.01}$	41^{+2}_{-3}	–	–	1.86	–	1.86	1.18(388)
7	022	57818.61	57831.99	$0.70^{+0.02}_{-0.02}$	$1.68^{+0.01}_{-0.01}$	47^{+4}_{-3}	–	–	2.19	–	2.19	0.99(401)
8	025	57832.02	57835.98	$0.67^{+0.02}_{-0.02}$	$1.70^{+0.02}_{-0.02}$	52^{+9}_{-6}	–	–	1.60	–	1.60	0.89(410)
9	026	57836.02	57840.96	$0.57^{+0.02}_{-0.02}$	$1.75^{+0.02}_{-0.02}$	50^{+7}_{-5}	–	–	2.42	–	2.42	0.90(359)
10	027	57841.00	57848.00	$0.58^{+0.02}_{-0.02}$	$1.77^{+0.02}_{-0.02}$	60^{+10}_{-7}	–	–	2.34	–	2.34	1.03(415)
11[a]	030	57848.06	57853.97	$0.59^{+0.01}_{-0.01}$	$1.79^{+0.01}_{-0.01}$	52^{+5}_{-4}	$0.40^{+0.02}_{-0.02}$	$14.1^{+1.5}_{-1.5}$	2.25	0.13	2.12	1.12(3411)
12[a]	032	57854.02	57855.96	$0.59^{+0.01}_{-0.01}$	$1.83^{+0.02}_{-0.02}$	58^{+13}_{-8}	$0.42^{+0.02}_{-0.02}$	$15.6^{+1.5}_{-1.3}$	2.14	0.20	1.94	1.12(3411)
13[a]	034	57856.01	57860.00	$0.59^{+0.01}_{-0.01}$	$1.79^{+0.01}_{-0.01}$	52^{+7}_{-5}	$0.42^{+0.03}_{-0.03}$	$12.5^{+1.6}_{-1.1}$	1.85	0.12	1.73	1.12(3411)
14	035	57860.00	57876.96	$0.62^{+0.02}_{-0.02}$	$1.72^{+0.02}_{-0.02}$	56^{+7}_{-5}	–	–	1.81	–	1.81	1.00(262)
15	036	57877.00	57881.95	$0.71^{+0.01}_{-0.01}$	$1.72^{+0.01}_{-0.01}$	66^{+13}_{-9}	–	–	1.97	–	1.97	1.09(550)
16	037	57882.00	57894.97	$0.62^{+0.01}_{-0.01}$	$1.72^{+0.01}_{-0.01}$	57^{+7}_{-5}	–	–	1.79	–	1.79	0.96(563)
17[a]	038	57895.02	57898.94	$0.59^{+0.01}_{-0.01}$	$1.79^{+0.02}_{-0.02}$	54^{+12}_{-8}	$0.35^{+0.03}_{-0.03}$	$13.9^{+2.7}_{-2.0}$	1.32	0.07	1.24	1.12(3411)
18	039	57899.05	57901.32	$0.54^{+0.02}_{-0.02}$	$1.77^{+0.03}_{-0.03}$	73^{+40}_{-18}	–	–	1.17	–	1.17	1.11(287)
19	040	57902.27	57913.89	$0.59^{+0.02}_{-0.02}$	$1.76^{+0.02}_{-0.02}$	75^{+21}_{-13}	–	–	1.64	–	1.64	0.93(321)
20	043	57914.01	57932.96	$0.54^{+0.01}_{-0.01}$	$1.75^{+0.02}_{-0.02}$	80^{+24}_{-14}	–	–	1.47	–	1.47	0.96(380)
21[a]	045	57933.01	57938.95	$0.59^{+0.01}_{-0.01}$	$1.81^{+0.02}_{-0.02}$	>70	$0.34^{+0.01}_{-0.01}$	$21.6^{+2.8}_{-2.1}$	1.24	0.16	1.08	1.12(3411)
22[a]	047	57939.05	57951.97	$0.59^{+0.01}_{-0.01}$	$1.78^{+0.02}_{-0.02}$	90^{+41}_{-21}	$0.37^{+0.01}_{-0.01}$	$16.9^{+1.4}_{-1.3}$	1.13	0.14	0.99	1.12(3411)
23[a]	050	57952.09	57963.00	$0.59^{+0.01}_{-0.01}$	$1.88^{+0.03}_{-0.03}$	74^{+46}_{-19}	$0.50^{+0.01}_{-0.01}$	$15.2^{+0.7}_{-0.7}$	1.11	0.38	0.73	1.12(3411)
24[a]	052	57963.09	57966.98	$0.59^{+0.01}_{-0.01}$	$1.92^{+0.03}_{-0.04}$	>120	$0.45^{+0.01}_{-0.01}$	$14.7^{+0.8}_{-0.7}$	0.92	0.22	0.70	1.12(3411)
25[a]	056	57967.02	57977.99	$0.59^{+0.01}_{-0.01}$	$1.80^{+0.01}_{-0.03}$	>150	$0.21^{+0.02}_{-0.01}$	$42.7^{+12.1}_{-10.2}$	0.60	0.08	0.52	1.12(3411)
26	057	57978.08	57982.99	$0.51^{+0.02}_{-0.02}$	$1.74^{+0.02}_{-0.03}$	>122	–	–	0.46	–	0.46	0.95(278)
27	–	57983.06	58001.97	–	$1.65^{+0.05}_{-0.05}$	>56	–	–	0.24	–	0.24	0.90(25)
28	061	58002.03	58022.0	$0.72^{+0.08}_{-0.07}$	$1.66^{+0.05}_{-0.06}$	>58	–	–	0.12	–	0.12	1.08(71)
29	066	58022.0	58075.38	$0.70^{+0.07}_{-0.07}$	$1.68^{+0.06}_{-0.06}$	35^{+32}_{-10}	–	–	0.08	–	0.08	1.23(101)

Note: [a] broad-band spectra fitted all together keeping linked $N_{\rm H}$ and letting the other parameters to vary.

observed in combination with a constant $R_{\rm c}$ and an increase of $kT_{\rm in}$ (see Table 4 and Fig. 4c).

4.4 Radio and correlation with X-rays

In Fig. 7, we show the radio/X-ray luminosity correlation combining data made available by Bahramian et al. (2018) and references therein.[6] All X-ray luminosities are calculated in the 1–10 keV energy range. We also added a simultaneous XRT (in HS, see Del Santo et al. 2016) and radio observation performed on MJD 56187.99 of the source *Swift* J174510.8–262411 (hereafter *Swift* J1745–26) that has been never taken into account in previous radio/X-ray luminosity correlation planes. We estimated a X-ray luminosity for *Swift* J1745–26 of 4.4×10^{37} erg s^{-1} at a distance of 7 kpc (Muñoz-Darias et al. 2013) and we used the 5 GHz radio flux density from Curran et al. (2014).

We measured the X-ray flux of GRS 1716–249 in the 1–10 keV energy band, using data that were quasi-simultaneous with the radio observations performed at $\sim$5 and $\sim$9 GHz (see Table 3). We

estimated X-ray luminosities ($d = 2.4$ kpc) of 2.8×10^{36} erg s^{-1} on MJD 57793, 4.4×10^{36} erg s^{-1} on MJD 57805, 2.8×10^{36} erg s^{-1} on MJD 57865, 9.4×10^{35} erg s^{-1} on MJD 57977, and 7.0×10^{35} erg s^{-1} on MJD 57978. GRS 1716–249 is located on the branch consistent with the slope of 1.4.

The radio spectral indices measured by ATCA at the beginning ($\alpha = -0.15 \pm 0.08$ on MJD 57793.835) and close to the end of the outburst ($\alpha = -0.07 \pm 0.19$ on MJD 57977.256) by VLA are both consistent with a flat-spectrum compact jet. Espinasse & Fender (2018) performed a study on a sample of 17 bright BHBs in HS. They show that the radio spectral indices distribution could be related to the position of the sources on the radio/X-ray luminosity correlation plane (see Section 5).

5 DISCUSSION

GRS 1716–249 increases the sample of X-ray binaries that have shown 'failed' state transitions outburst, in which the source does not complete the full *q*-track pattern in the HID. In spite of the three softening events that occurred during the outburst, GRS 1716–249 did not make the transition to the canonical SS (neither to the
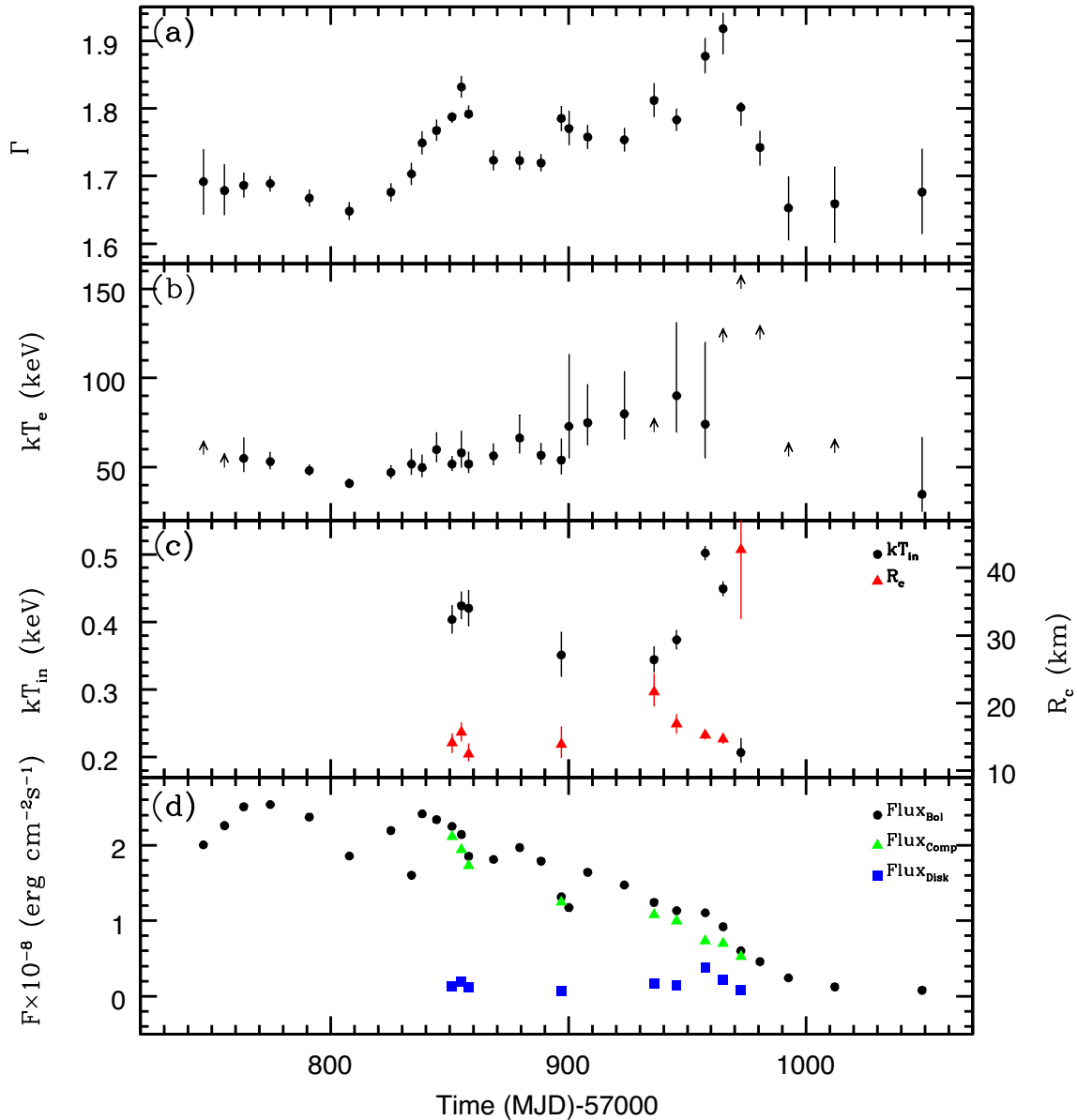
Figure 4. Evolution of the main spectral parameters and flux obtained fitting the broad-band spectra with an absorbed thermal Comptonization model (TBABS∗NTHCOMP) plus a disc black-body component (DISKBB) when required (parameters reported in Table 4). From the top to the bottom panel: (a) photon index, (b) Comptonizing electron temperature in units of keV, (c) inner disc black-body temperature in units of keV (black dots) and inner disc radius depending on the inclination angle (R_c) in units of km (red triangles), and (d) 0.1–500 keV unabsorbed bolometric flux in units of 10^{-8} er g cm^{-2} s^{-1} (black dots). The green triangles show the Comptonized flux and the blue squares show the disc flux. The disc luminosity never dominates the energetic of the source.

SIMS). This is supported by two findings: the disc luminosity never dominates the emission of the source and the fractional rms never decreases below 10 per cent.

Tetarenko et al. (2016) reported on an all-sky data base of galactic BHTs. They found that ∼40 per cent of sources are 'hard only', including also sources showing 'failed' state transition outbursts (i.e. HS-HIMS only). These authors suggest that the mass transfer rate ($\dot{M}$) over the all outburst could be insufficient to allow the source to perform the transition to the SSs. Indeed, they found that all 'hard only' sources show outburst peak luminosities lower than $0.11\,L_{Edd}$. The peak bolometric luminosity of GRS 1716–249 (L_{peak} ∼0.03 L_{Edd}) is in agreement with their limit. On the other hand, the 'failed' state transition source *Swift* J1745–26 (Del Santo et al. 2016) showed L_{peak} ∼0.37 L_{Edd} (d ∼7 kpc; Muñoz-Darias et al.

2013), which is more than a factor of 3 higher than the upper limit reported in Tetarenko et al. (2016). This would suggest that the overall mass-transfer rate during the outburst is not the only parameter involved in the 'failed' state transition behaviour or that the limit is higher than what Tetarenko et al. (2016) thought.

However, even though the most widely accepted distance of *Swift* J1745–26 is 7 kpc (Curran et al. 2014; Kalemci et al. 2014), this value is poorly constrained (Muñoz-Darias et al. 2013). Thus, if we assume a distance lower than ∼4 kpc, even the BHT *Swift* J1745–26 would fall within the proposed upper limit of 0.11 L_{Edd}.

In the truncated disc model scenario, the inner radius of the accretion disc is smaller when we observe softer spectra. In GRS 1716–249, this occurs up to a certain point when kT_{in} starts to increase at constant inner disc radius. Thus, we argue that GRS
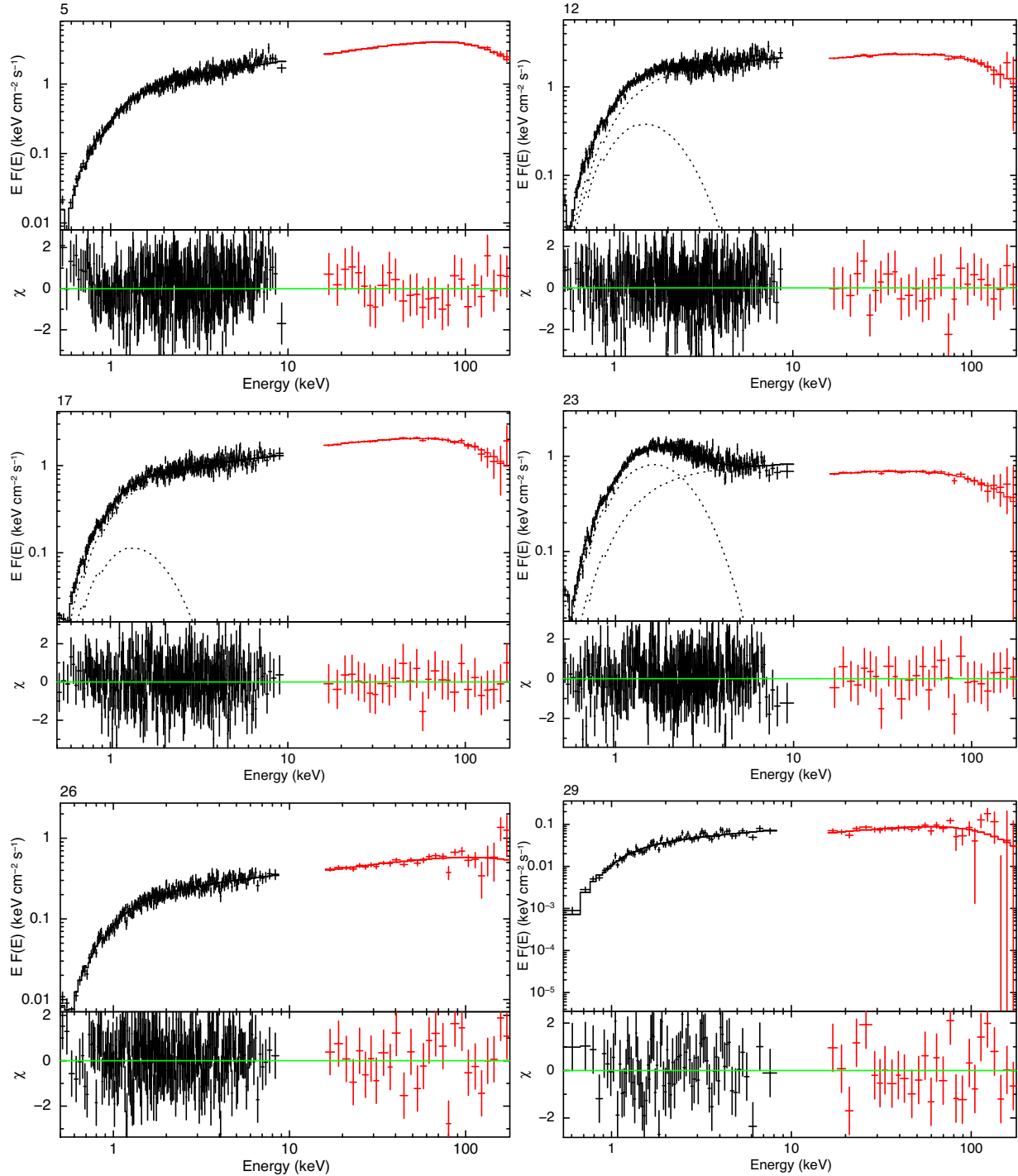
Figure 5. Broad-band energy spectra of six different XRT pointings (#5, #32, #38, #50, #57, and #66, see Table 1) with average BAT spectra in the corresponding quasi-simultaneous GTIs. They are fitted with an absorbed thermal Comptonization model (TBABS∗NTHCOMP) plus a multicolour disc black-body component (DISKBB) when required (*12, 17,* and *23*). The spectral parameters are reported in Table 4 (spectra *5, 12, 17, 23, 26,* and *29*).

1716–249 might have reached the ISCO in the HIMS. We folded the XRT light curves at the binary system period (∼14.7 hr), covering about ∼80 per cent of this, and we did not find any evidence for dips and/or eclipses. In addition, we also folded the *INTEGRAL*/JEM-X light curve (3–6 keV) collected during the 96 ks of *INTEGRAL* ToO triggered by our team during a multiwavelength campaign in the HS (results on this will be presented in a further paper). This light curve covered ≈100 per cent of the binary period and even in this

case we did not find any evidence of features indicative of a high inclination system for GRS 1716–249, which is likely to be ruled out. Assuming an inclination angle the upper limit $\vartheta < 60°$ (Frank, King & Lasota 1987) and using the inner disc radius $R_c \sim 15$ km, we obtain an upper limit $R_{ISCO} < 21$ km. The lower limit on the BH mass ($M_{BH} > 4.9\,M_\odot$; Masetti et al. 1996) allows us to estimate a lower limit on the gravitational radius as $R_g > 7.3$ km that results in a $R_{ISCO} < 3\,R_g$. In the Schwarzschild metric $R_{ISCO} = 6\,R_g$, therefore
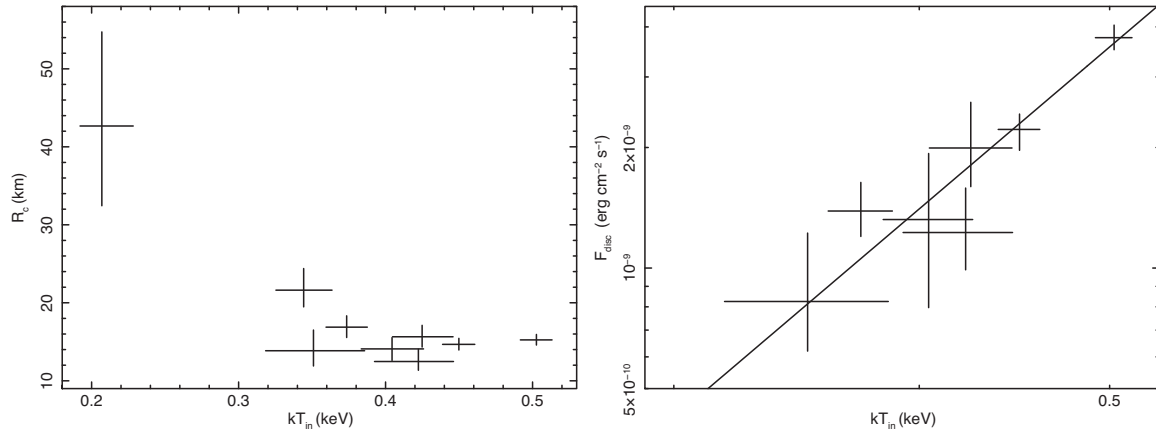
Figure 6. *Left-hand panel:* Inner disc radius depending on the inclination angle (R_c) in function of the inner disc temperature. R_c decreases with the increase of the temperature until it reaches an almost constant value. *Right-hand panel:* The observed disc flux versus the inner disc temperature including only spectra with R_c almost constant. The slope of the power law in log–log is $\alpha = 4.2 \pm 1.0$, in agreement with a constant inner disc radius scenario.
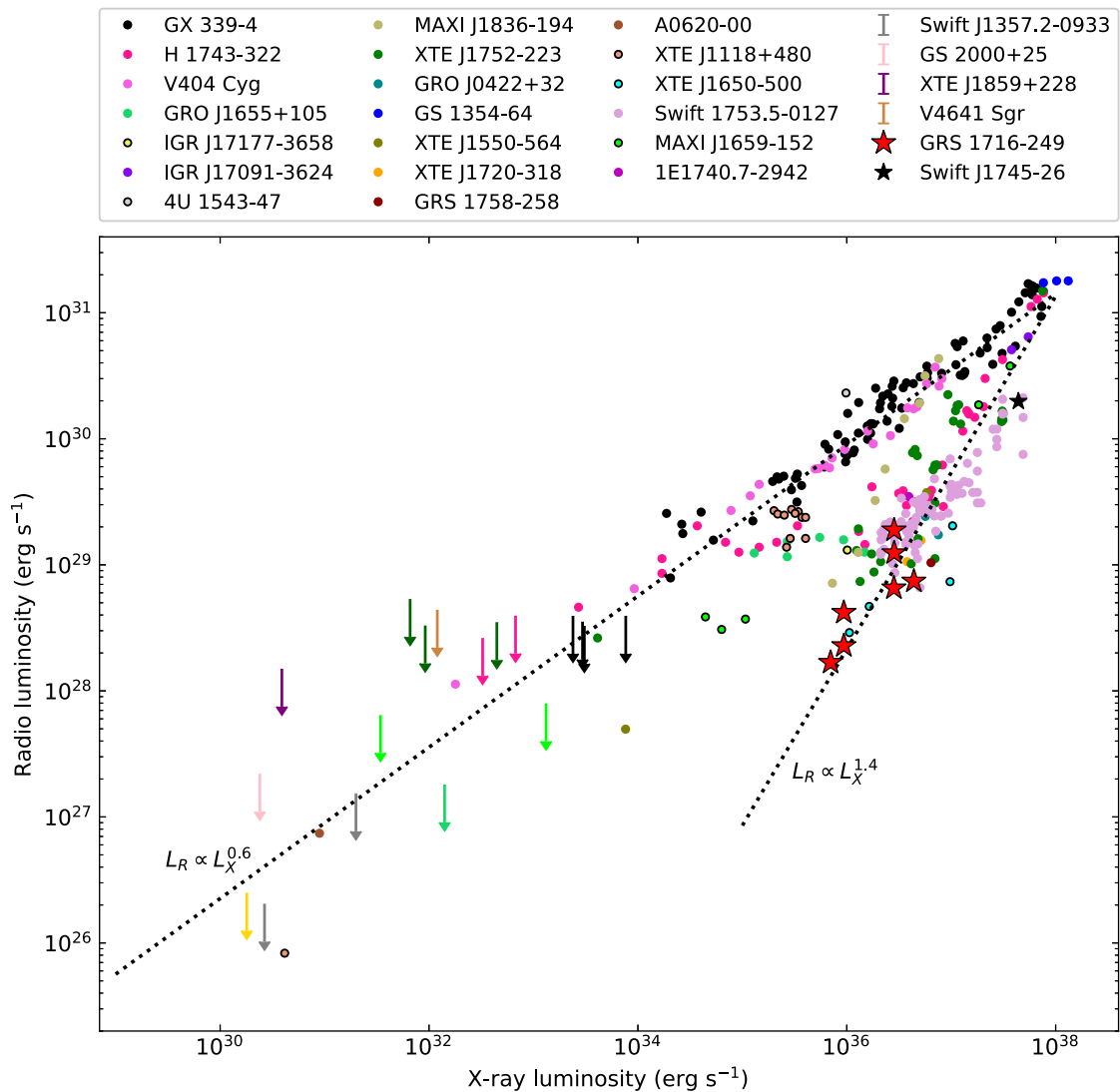

Figure 7. Radio/X-ray luminosity correlation. The X-ray luminosities have been calculated in the 1–10 keV energy range and the radio observations, collected at different frequencies, have been converted by Bahramian et al. (2018) to a common radio frequency, i.e. ∼5 GHz. GRS 1716–249 (red stars) is located on the radio-quiet branch. For this source we plotted radio observations performed both at ∼5 and ∼9 GHz.

the BH in GRS 1716–249 would be rotating with a spin lower limit of $a_* > 0.8$ (with a_* the dimensionless spin). We are aware that this is only a rough estimation, due to the extreme simplicity of the disc model used in this paper.

The radio emission of GRS 1716–249 is consistent with coming from a compact jet, despite R_{in} being at the ISCO. However, we do not have an adequate radio coverage (e.g. a regular radio sample or VLBI observations) during the outburst and in particular during the soft episodes. It is worth noting that, it does not appear that GRS 1716–249 got soft enough to quench the compact jet and to create transient ejecta (Fender, Belloni & Gallo 2004). The radio observations were performed when GRS 1716–249 was in HS-HIMS (see Section 3). We cannot exclude that the jet changed its properties when the X-ray emission became softer and that there were rapid ejection events, quenching or steepening episodes we did not observe. This imply that the jet could be recovered in short times, between one radio observation and the next one.

An important tool to investigate the emission properties of BHTs is the radio/X-ray correlation. Coriat et al. (2011) suggested that the radio/X-ray correlation of the 'outliers' (or radio-quiet BHTs with $L_R \propto L_X^{1.4}$) is produced by a radiatively efficient accretion flow. It means that $L_X \propto \dot{M}$, while the radio-loud branch ($L_R \propto L_X^{0.6}$) would result from inefficient accretion where $L_X \propto \dot{M}^{2-3}$. Both GRS 1716–249 and *Swift* J1745–26 are located on the steeper branch and they increase the number of radio-quiet BHTs. Recently, the accretion efficiency picture proposed to explain the two different branches is challenged by the recent finding that radio-quiet tend to have a negative spectral index α ($S_\nu \propto \nu^\alpha$), while for the radio-loud sources a positive α was observed. This suggests different core jet properties (rather than accretion flow) for the two classes of sources (Espinasse & Fender 2018). Furthermore, we observe that the source never left the radio-quiet branch, again arguing against a quenching by the jet.

The power-law slopes of the GRS 1716–249 radio spectra, as also the *Swift* J1745–26 radio slope ($\alpha \sim 0$; Curran et al. 2014), are within the statistical distribution of the radio-quiet slope reported by Espinasse & Fender (2018).

Recently, Motta et al. (2018) proposed that the origin of different radio loudness of BHTs is due to the geometric effects due to the inclination of the sources: i.e the radio-quiet sources would be at high inclination. However, GRS 1716–249 is a radio-quiet system most likely at low inclination. Nevertheless dips can be transient as observed in H 1743–322 (Motta et al. 2015 and references therein), so the low inclination of GRS 1716–249 has to be confirmed. The radio-quiet/X-ray-bright behaviour of the source might be related to the very small inner disc radius that we infer from our disc modelling. Indeed, the small inner disc radius does not necessarily imply the disc extends uninterrupted from its outer parts and down to the ISCO. Coupled disc/corona condensation evaporation models, developed in the framework of the truncated disc model, predict that when the sources are close to IMS, the inner hot-flow may re-condensate into an inner cool ring that would present observational signatures that are very similar to that of a full disc (Meyer-Hofmeister, Liu & Meyer 2009). Then, the contribution from the soft photons of the disc would make the accretion flow brighter in X-rays with respect to an accretion flow at the same accretion rate (and therefore radio luminosity) in which this mini inner-disc would be absent. Meyer-Hofmeister & Meyer (2014) argue that this could drive the different slope of the radio X-ray correlation of radio-quiet sources. Our results appear to be consistent with their picture.

6 CONCLUSIONS

In this work, we have presented the X-ray spectral and timing analysis of the BHT GRS 1716–249 during its 2016–2017 outburst. We analysed the XRT and BAT observations collected during the whole outburst occurred from December 2016 to October 2017. In addition, we have reported on five radio observations and their correlation with X-ray data. Our main results can be summarized as follows:

(1) GRS 1716–249 can be added at the sample of the known BHTs that show a 'failed' state transition outburst. During the outburst the source showed three softer episodes without making the transition to the SS. Timing results and spectral parameters evolution are consistent with the source being in the HS at the beginning and at the end of the outburst, and in the HIMS during the spectral softening.

(2) Our data suggest that the inner disc might have reached the ISCO during the three softening episodes, even-though the source was in the HIMS. However, disc/corona condensation-evaporation models predict that in the intermediate state the hot accretion flow may re-condensate into an inner mini-disc, mimicking the emission of the full disc.

(3) The source might host a rapidly rotating BH with a rough spin lower limit of 0.8.

(4) In the radio/X-ray luminosity plane GRS 1716–249 is located on the radio-quiet branch, which is in agreement with the X-ray brightness due to the condensed inner accretion flow.

REFERENCES

Bahramian A. et al., 2018, Radio/X-ray Correlation Database for X-ray Binaries (v0.1). Available at: http://doi.org/10.5281/zenodo.1252036

Ballet J., Denis M., Gilfanov M., Sunyaev R., Harmon B. A., Zhang S. N., Paciesas W. S., Fishman G. J., 1993, IAU Circ., 5874

Barthelmy S. D. et al., 2005, Space Sci. Rev., 120, 143
Belloni T. et al., 2006, MNRAS, 367, 1113
Belloni T. M., Motta S. E., 2016, in Bambi C., ed., Astrophysics and Space Science Library, Astrophysics of Black Holes: From Fundamental Aspects to Latest Developments, Vol. 440, Springer-Verlag, Berlin, p. 61
Belloni T. M., Motta S. E., Muñoz-Darias T., 2011, Bull. Astron. Soc. India, 39, 409
Blandford R. D., Königl A., 1979, ApJ, 232, 34
Burrows D. N. et al., 2005, Space Sci. Rev., 120, 165
Capitanio F., Belloni T., Del Santo M., Ubertini P., 2009, MNRAS, 398, 1194
Corbel S., Fender R. P., 2002, ApJ, 573, L35
Corbel S., Fender R. P., Tzioumis A. K., Nowak M., McIntyre V., Durouchoux P., Sood R., 2000, A&A, 359, 251
Corbel S., Nowak M. A., Fender R. P., Tzioumis A. K., Markoff S., 2003, A&A, 400, 1007
Corbel S., Coriat M., Brocksopp C., Tzioumis A. K., Fender R. P., Tomsick J. A., Buxton M. M., Bailyn C. D., 2013, MNRAS, 428, 2500
Coriat M. et al., 2011, MNRAS, 414, 677
Curran P. A. et al., 2014, MNRAS, 437, 3265
Del Santo M. et al., 2009, MNRAS, 392, 992
Del Santo M. et al., 2016, MNRAS, 456, 3585
Del Santo M., D'Ai' A., Bassi T., Segreto A., Belloni T., Cusumano G., La Parola V., 2017a, Astron. Telegram, 10036
Del Santo M. et al., 2017b, Astron. Telegram, 10069
della Valle M., Mirabel I. F., Cordier B., Bonibaker J., Stirpe G., Rodriguez L. F., 1993, IAU Circ., 5876
della Valle M., Mirabel I. F., Rodriguez L. F., 1994, A&A, 290, 803
Deller A. T. et al., 2011, PASP, 123, 275
Done C., Gierliński M., Kubota A., 2007, A&AR, 15, 1
Dunn R. J. H., Fender R. P., Körding E. G., Belloni T., Cabanac C., 2010, MNRAS, 403, 61
Espinasse M., Fender R., 2018, MNRAS, 473, 4122
Evans P. A. et al., 2007, A&A, 469, 379
Evans P. A. et al., 2009, MNRAS, 397, 1177
Fender R. et al., 1999, ApJ, 519, L165
Fender R. P., Hjellming R. M., Tilanus R. P. J., Pooley G. G., Deane J. R., Ogley R. N., Spencer R. E., 2001, MNRAS, 322, L23
Fender R. P., Belloni T. M., Gallo E., 2004, MNRAS, 355, 1105
Fender R. P., Stirling A. M., Spencer R. E., Brown I., Pooley G. G., Muxlow T. W. B., Miller-Jones J. C. A., 2006, MNRAS, 369, 603
Ferrigno C., Bozzo E., Del Santo M., Capitanio F., 2012, A&A, 537, L7
Frank J., King A. R., Lasota J.-P., 1987, A&A, 178, 137
Gallo E., Fender R. P., Pooley G. G., 2003, MNRAS, 344, 60
Gehrels N. et al., 2004, ApJ, 611, 1005
Greisen E. W., 2003, in Heck A., ed., Astrophysics and Space Science Library Vol. 285, Information Handling in Astronomy – Historical Vistas, AIPS, the VLA, and the VLBA, Vol. 285, Kluwer Academic Publishers, Dordrecht, p. 109
Harmon B. A., Fishman G. J., Paciesas W. S., Zhang S. N., 1993, IAU Circ., 5900

Hjellming R. M., Rupen M. P., Shrader C. R., Campbell-Wilson D., Hunstead R. W., McKay D. J., 1996, ApJ, 470, L105
Homan J., Belloni T., 2005, Ap&SS, 300, 107
Kalemci E. et al., 2014, MNRAS, 445, 1288
Kubota A., Tanaka Y., Makishima K., Ueda Y., Dotani T., Inoue H., Yamaoka K., 1998, PASJ, 50, 667
Laurent P., Titarchuk L., 1999, ApJ, 511, 289
Leahy D. A., Elsner R. F., Weisskopf M. C., 1983, ApJ, 272, 256
Masetti N., Bianchini A., Bonibaker J., della Valle M., Vio R., 1996, A&A, 314, 123
Masumitsu T. et al., 2016, Astron. Telegram, 9895
McMullin J. P., Waters B., Schiebel D., Young W., Golap K., 2007, in Shaw R. A., Hill F., Bell D. J., eds, ASP Conf. Ser. Vol. 376, Astronomical Data Analysis Software and Systems XVI. Astron. Soc. Pac., San Francisco, p. 127
Meyer-Hofmeister E., Meyer F., 2014, A&A, 562, A142
Meyer-Hofmeister E., Liu B. F., Meyer F., 2009, A&A, 508, 329
Mirabel I. F., 1994, ApJS, 92, 369
Motta S., Belloni T., Homan J., 2009, MNRAS, 400, 1603
Motta S. E., Casella P., Henze M., Muñoz-Darias T., Sanna A., Fender R., Belloni T., 2015, MNRAS, 447, 2059
Motta S. E., Casella P., Fender R. P., 2018, MNRAS, 478, 5159
Muñoz-Darias T., Motta S., Belloni T. M., 2011, MNRAS, 410, 679
Muñoz-Darias T. et al., 2013, MNRAS, 432, 1133
Negoro H. et al., 2016, Astron. Telegram, 9876
Niedźwiecki A., Zdziarski A. A., 2006, MNRAS, 365, 606
Poutanen J., Coppi P. S., 1998, Phys. Scr. Vol. T, 77, 57
Remillard R. A., McClintock J. E., 2006, ARA&A, 44, 49
Romano P. et al., 2006, A&A, 456, 917
Sault R. J., Teuben P. J., Wright M. C. H., 1995, in Shaw R. A., Payne H. E., Hayes J. J. E., eds, ASP Conf. Ser. Vol. 77, Astronomical Data Analysis Software and Systems IV. Astron. Soc. Pac., San Francisco, p. 433
Segreto A., Cusumano G., Ferrigno C., La Parola V., Mangano V., Mineo T., Romano P., 2010, A&A, 510, A47
Shakura N. I., Sunyaev R. A., 1973, A&A, 24, 337
Shimura T., Takahara F., 1995, ApJ, 445, 780
Soleri P. et al., 2013, MNRAS, 429, 1244
Tanaka Y., 1993, IAU Circ., 5877
Tetarenko B. E., Sivakoff G. R., Heinke C. O., Gladstone J. C., 2016, ApJS, 222, 15
Verner D. A., Ferland G. J., Korista K. T., Yakovlev D. G., 1996, ApJ, 465, 487
Wilms J., Allen A., McCray R., 2000, ApJ, 542, 914
Zdziarski A. A., 2000, in Martens P. C. H. Tsuruta S., Weber M. A., eds, Highly Energetic Physical Processes and Mechanisms for Emission from Astrophysical Plasmas, Vol. 195, Astronomical Society of the Pacific, San Francisco, p. 153
Zdziarski A. A., Gierliński M., 2004, Prog. Theor. Phys. Suppl., 155, 99

This paper has been typeset from a TEX/LATEX file prepared by the author.